Myhill, R. C., Frost, D. J., & Novella, D. (2017). Hydrous melting and partitioning in and above the mantle transition zone: insights from water-rich MgO-SiO2-H2O experiments. *Geochimica et Cosmochimica Acta*, *200*, 408-421. https://doi.org/10.1016/j.gca.2016.05.027

Hydrous melting and partitioning in and above the mantle transition zone: insights from water-rich MgO-SiO_2-H_2O experiments

R. Myhill, D. J. Frost

Bayerisches Geoinstitut, Universität Bayreuth, Universitätsstrasse 30, 95447 Bayreuth, Germany

D. Novella

Laboratoire Magmas et Volcans, Université Blaise Pascal, 5 Rue Kessler, 63038 Clermond-Ferrand, France

Abstract

Hydrous melting at high pressures affects the physical properties, dynamics and chemical differentiation of the Earth. However, probing the compositions of hydrous melts at the conditions of the mantle transition zone has traditionally been challenging. In this study, we conducted high pressure multianvil experiments at 13 GPa between 1200 and 1900 °C to investigate the liquidus in the system MgO-SiO_2-H_2O. Water-rich starting compositions were created using platinic acid ($H_2Pt(OH)_6$) as a novel water source. As MgO:SiO_2 ratios decrease, the T-X_{H_2O} liquidus curve develops an increasingly pronounced concave-up topology. The melting point reduction of enstatite and stishovite at low water contents exceeds that predicted by simple ideal models of hydrogen speciation. We discuss the implications of this work on the behaviour of melts in the deep upper mantle and transition zone, and present new models describing the partitioning of water between the olivine polymorphs and associated hydrous melts.

Keywords: high pressure, mantle, hydrous melting, water, liquidus

*Corresponding author: R. Myhill
Email address: myhill.bob@gmail.com (R. Myhill, D. J. Frost)

1. Introduction

Hydrous melts have a remarkable influence on Earth's surface and interior. Melting at subduction zones is primarily driven by the release of hydrous fluids from the warming slab at about 100 km depth, producing the world's arc volcanoes. The water cycle does not stop here, however; hydrous minerals within the crust should allow some water to be transported to 250 km (Poli and Schmidt, 2002), and peridotite hydration should allow water to penetrate into the mantle transition zone or deeper, providing it remains low enough in temperature (Komabayashi et al., 2005). This deep water cycle must extend to at least 500 km depth, as implied by the discovery of water-saturated ringwoodite in a diamond from Juina, Brazil (Pearson et al., 2014). In addition to kimberlites and arc volcanoes, hydrous melts are known to metasomatise and refertilise the lithospheric mantle, creating the so-called MARID (mica, amphibole, rutile, ilmenite, diopside) assemblage. It has also been argued that neutral or negatively buoyant water-rich melts are to blame for low velocity and high conductivity layers observed at the 410 km discontinuity, and that these small fraction melts could act to filter out incompatible elements during upwelling (Bercovici and Karato, 2003).

Processes involving deep-seated hydrous melts are controlled to a great extent by melt composition. Most importantly, the equilibrium proportion of H_2O in melts controls the melt fraction for a given bulk H_2O content. Together with solid-solid-melt dihedral angles, the extent of partial melting governs the permeability and therefore mobility of melt, and the ability to detect it via body wave seismology and electrical conductivity measurements. Melt densities and viscosities are also governed by their composition. Finally, changes in equilibrium melt composition with pressure, temperature and bulk composition can enhance melt channelisation, which reduces melt-solid interaction and increases ascent rates (e.g. Spiegelman et al., 2001; Weatherley and Katz, 2012).

Melt compositions are also required to understand the stability of dense hydrous magnesium silicate (DHMS) phases and the water capacity of nominally

anhydrous minerals (NAMS) at high pressure. Together, these control water transport and storage in the deep mantle, and as such are the primary inputs to models of the water budget of the Earth (Hirschmann, 2006). Hydrous fluids at elevated pressures and temperatures cannot be treated as pure H_2O. As pressure increases, immiscibility between fluid and melt decreases, and the thermal stability of hydrous phases increases. As a result, fluids/melts released by the breakdown of hydrous phases have H_2O activities significantly lower than one. Understanding and predicting the P-T conditions of DHMS phase breakdown and the water storage capacity at of NAMS therefore requires good activity-composition models for hydrous melts.

Constraining melt compositions remains a major challenge in high-pressure experimental petrology. The primary problem is that water-rich melts are unquenchable. During quench, some of the water in the melt crystallises as hydrous minerals such as brucite, but a significant proportion crystallises as water ice at high pressure, which is then lost as water vapour on decompression and during sample preparation. The original H_2O contents of the partial hydrous melts are normally estimated by mass balance and/or by deficits in microprobe totals (e.g. Ohtani et al., 2000; Demouchy et al., 2005; Litasov et al., 2011; Melekhova et al., 2007). Mass balance alone depends on being able to accurately estimate the volume proportions of solid phases and quench phases, recognise and subtract quench overgrowths where they exist, and calculate the effective ambient-pressure density of the melt. All of these are associated with significant uncertainties. Deficits in microprobe totals are sometimes reasonable for estimating water contents in solid phases, provided the microprobe standards are suitable, and the microprobe is exceptionally well-calibrated (even a small deficit implies a large water content). However, for quench melts the deficits are attributable to water held in quench phases *and* porosity within the volume sampled by the defocused beam. For this reason, defocused beam techniques should probably be restricted to estimating non-volatile element ratios (such as Mg:Si).

Here we use the approach of bracketing the liquidus surface to determine melt

composition as a function of temperature in the system MgO-SiO_2-H_2O (MSH). This technique requires knowledge of the starting composition, techniques to effectively minimise water loss from the capsule and an ability to recognise the difference between liquidus and quench phases. We use this technique to develop thermodynamic models for water solubility in melts, and apply these to models of water partitioning between mantle phases and melts. We then apply these models to better understand hydrous melting under transition zone conditions.

2. Experimental and analytical methods

Starting compositions were created from a mixture of high-purity brucite, quartz and platinic acid (hexahydroxyplatinate(IV); $H_2Pt(OH)_6$). We use platinic acid to increase water contents to those expected of hydrous melts in equilibrium with mantle phases under subduction/convecting mantle conditions. Platinic acid is a pale yellow compound which is stable to about 130 °C (Nagano, 2002). Its relatively high stability, high water content and the inert nature of the breakdown product (in a system where redox reactions are absent) make it an excellent water source for high pressure hydrous melting experiments. Before weighing, quartz was dried at 1000 °C for 12 hours, while brucite was heated to 250 °C, also over 12 hours. Both powders were stored in a desiccating oven at 130 °C. Platinic acid is hygroscopic, so was stored in a vacuum desiccator. Powders were weighed and ground dry in an agate mortar for 30 minutes, using a mask, goggles and gloves to avoid physical contact with the platinic acid. Prepared powders were stored in glass vials in a vacuum desiccator until use.

We chose starting compositions to cover the brucite-quartz-water subregion of the MSH ternary. Chosen compositions include points on the binaries between water and brucite, forsterite, enstatite and stishovite, and a few additional compositions to constrain the locations of cotectics (Table 1).

Capsules were created from 2 mm-diameter $Pt_{90}Rh_{10}$ and Au rods, cut by wire saw into 1 mm thick disks. Into each disk were spark-eroded two rows of three holes, each 250 microns in diameter and 700 microns deep. The capsules

Table 1: Starting compositions

	Oxide proportions (mol%)			Compound fractions (mol/mol)		
	MgO	SiO_2	H_2O	$Mg(OH)_2$	SiO_2	$H_2Pt(OH)_6$
br 5.0	50.000	0.000	50.000	1.000	0.000	0.000
br 5.5	45.000	0.000	55.000	0.947	0.000	0.053
br 6.0	40.000	0.000	60.000	0.889	0.000	0.111
br 6.5	35.000	0.000	65.000	0.824	0.000	0.176
br 7.0	30.000	0.000	70.000	0.750	0.000	0.250
en 6.0	30.000	30.000	40.000	0.480	0.480	0.040
en 7.0	26.667	26.667	46.667	0.457	0.457	0.086
en 8.0	23.333	23.333	53.333	0.431	0.431	0.138
en 9.0	20.000	20.000	60.000	0.400	0.400	0.200
fo 11.5	36.000	18.000	46.000	0.637	0.319	0.044
fo 13.0	32.000	16.000	52.000	0.604	0.302	0.094
fo 14.5	28.000	14.000	58.000	0.566	0.283	0.152
fo 16.0	24.000	12.000	64.000	0.522	0.261	0.217
q 1.5	0.000	85.000	15.000	0.000	0.958	0.042
q 2.0	0.000	80.000	20.000	0.000	0.941	0.059
q 2.5	0.000	75.000	25.000	0.000	0.923	0.077
q 3.0	0.000	70.000	30.000	0.000	0.903	0.097
q 3.5	0.000	65.000	35.000	0.000	0.881	0.119
q 4.0	0.000	60.000	40.000	0.000	0.857	0.143
q 4.5	0.000	55.000	45.000	0.000	0.830	0.170
q 5.0	0.000	50.000	50.000	0.000	0.800	0.200
br+q 2.25	25.000	50.000	25.000	25.000	50.000	0.000
br+q 2.70	30.000	40.000	30.000	30.000	40.000	0.000
br+q 3.2	35.556	28.889	35.556	35.556	28.889	0.000
br+q 3.4	37.778	24.444	37.778	37.778	24.444	0.000

were cleaned by cycling between an acetone ultrasonic bath (15 minutes) and 1000 °C furnace (20 minutes) three times. Any remaining contamination was removed with a $W_{75}Re_{25}$ needle followed by a further trip to the ultrasonic bath. Capsule chambers were filled with powders of different compositions using a $W_{75}Re_{25}$ needle. Small pieces of tape were used to temporarily cover the other holes to avoid contamination.

Multianvil experiments were performed in the 5000 tonne press at the Bayerisches Geoinstitut (BGI). Cr-doped MgO octahedral multianvil assemblies with 18 mm edge length were used (Figure 1). Two capsules were loaded into each assembly, with the open ends of the chambers facing each other and separated by six 0.05 mm thick $Pt_{90}Rh_{10}$ or Au foils. The assemblies were compressed to 13 GPa over four hours between eight tungsten carbide cubes with trucations of edge-length 11 mm. Pressure calibrations and details of the press can be found in Frost et al. (2004) and Keppler and Frost (2005). The assemblies were then resistively heated via a stepped $LaCrO_3$ heater. The temperature was recorded using a $W_{97}Re_3$–$W_{75}Re_{25}$ (Type D) thermocouple inserted axially into the assembly. To avoid water loss, higher temperature runs were heated for a shorter duration (see Novella et al., 2016). The experiments were quenched by cutting power to the heater. The assemblies were then decompressed to room pressure over 1000 minutes.

Capsules were recovered from the assembly, separated by wire saw and then ground by hand to reveal the tops of each capsule chamber. The wire saw was then used again to split the two sets of three chambers from each capsule. Each half-capsule was mounted in epoxy and mirror-polished. After revealing the edge of the capsule chambers, it was necessary to impregnate them with epoxy under vacuum before further polishing, in order to fill in the porous spaces created by the hydrous melt. Grinding under running water helped remove plucked grains from the polishing surface. Prepared and cleaned samples were then coated with a 10 nm thick carbon layer.

Analysis of run products was conducted via scanning electron microscope (SEM), using BSE imaging and EDS for phase identification (via the INCA

software package).

3. Modelling water solubility in melts

3.1. Background

Oxygen in neutral MSH melt species can exist either as molecular water, as a bridging oxygen between magnesium and/or silicon atoms, or as part of a terminal hydroxyl group. The general equation describing the reaction between melt species is

$$\mathrm{H_2O} + \mathrm{O}_{br}^{2-} \rightleftharpoons 2\mathrm{OH}_{tm}^{-} \tag{1}$$

where the subscripts br and tm respectively refer to bridging and terminal oxygens. The equilibrium between these species can be described with an equilibrium constant K (e.g. Stolper, 1982)

$$K_{(1)} = \frac{X_{\mathrm{OH}_{tm}^{-}}{}^{2}}{X_{\mathrm{H_2O}} X_{\mathrm{O}_{br}^{2-}}} \tag{2}$$

The equilibrium constant is related to the energy $\Delta G_{(1)}$ required to create two terminal OH groups from a bridging oxygen and a water molecule

$$K_{(1)} = \exp\left(\frac{-\Delta G_{(1)}}{RT}\right) \tag{3}$$

These equations can be used to describe in an average sense a range of melt-melt equilibria involving monomers ($\mathrm{Mg(OH)_2}$ and $\mathrm{Si(OH)_4}$), dimers ($\mathrm{Mg_2O(OH)_2}$, $\mathrm{MgSiO(OH)_4}$, $\mathrm{Si_2O(OH)_6}$) and higher oligomers. A high proportion of monomers and dimers exist in relatively dilute solutions, but not in the concentrated solutions investigated in this study.

A number of models have been presented to investigate the behaviour of water-bearing silicate melts. Silver and Stolper (1985) made the assumption that $\mathrm{H_2O}$, O_{br}^{2-} and OH_{tm}^{-} mix ideally, with a parameter r representing the number of oxygen atoms in each formula unit which are available for protonation. For example, an $\mathrm{Mg_2SiO_4}$ melt with $r = 4$ and $K_{(1)} = \infty$ represents a continuum between an anhydrous melt and one made of $\mathrm{Mg(OH)_2}$ and $\mathrm{Si(OH)_4}$

monomers. No distinction is made between isolated oligomers and partial depolymerisation of a silicate network; in other words, the energy required to form a terminal OH group is independent of local environment. Fixing r places an implicit constraint on the maximum value of $K_{(1)}$ in water-rich compositions. For example, if $r = 1$ in a hydrated MgO melt, then water contents exceeding 50 mol% require that $K_{(1)} < \infty$. In practise, the equilibrium constant $K_{(1)}$ has been shown to be dependent on temperature and composition. Shen and Keppler (1995) obtained a good fit to isochemical data with an expression of the form

$$\Delta G_{(1)} = a + b\,T \tag{4}$$

Tenner et al. (2012) simplified the model of Silver and Stolper (1985) by assuming that all hydrogen in the melt exists as OH^-, and that protonation is equally likely on any oxygen ($K_{(1)} = \infty$, $\Delta G_{(1)} = -\infty$, r maximised). Deviations from this model must increase with increasing water content, and such a model cannot describe any melt more water-rich than the $Mg(OH)_2$-$Si(OH)_4$ binary.

To describe melting in the SiO_2-H_2O system, Hunt and Manning (2012) generalised the aforementioned models by allowing non-ideality between the two endmembers. The excess term $\Delta G_{(1)}$(P,T) for the formation of OH^- groups was assumed to be independent of composition; all oxygens are equally available for protonation, and the local extent of protonation does not affect the energy required for each further protonation.

These models can be used to calculate solid-melt equilibria by equating the Gibbs free energy of the solid G^s_{solid} with the chemical potential of the melt component with the same composition μ^s_{melt}:

$$G^s_{solid} = \mu^s_{melt} = G^s_{melt} - RT \ln a^s_{melt} \tag{5}$$

In this study, we use the thermodynamic dataset of Stixrude and Lithgow-Bertelloni (2011) to calculate G^s_{solid} for periclase, forsterite and its high pressure polymorphs, orthoenstatite, high pressure clinoenstatite, coesite and stishovite. A modified version of the molecular dynamics-derived anhydrous melt model of

de Koker et al. (2013) is used to calculate G^s_{melt}, and the Silver and Stolper (1985) model is used to calculate a^s_{melt}. The calculations in the work were undertaken with the mineral physics toolkit Burnman (available from `https://geodynamics.org/cig/software/burnman/` Cottaar et al., 2014).

3.2. The anhydrous melt model

3.2.1. Endmembers

Thermodynamic models of MgO-SiO_2 melts are currently in their infancy. Many of the techniques used to constrain the thermodynamic properties (particularly the equations of state) of solids cannot be used on liquids as a result of their highly dynamic behaviour. Therefore in this study, we use MgO and SiO_2 melt models derived from molecular dynamics simulations (de Koker et al., 2013), and fit a simplified mixing curve based on experimental data. First, however, the thermodynamic properties of the endmember melts need to be adjusted to fit the experimentally derived thermodynamic data at the melting point. This step was unnecessary in the original study of de Koker et al. (2013) because solid properties were also obtained by molecular dynamics simulations. Such simulations do not provide good estimates of absolute energies and entropies, and so the values of the solids were obtained by fixing the melting point at a given pressure to the experimentally derived values (0 GPa, 3070 K for periclase, 14 GPa, 3120 K for stishovite). It turns out that the MD-determined entropy of periclase is almost identical to the experimentally determined values at all pressures and temperatures (Stixrude and Lithgow-Bertelloni, 2011), so we only needed to adjust the standard state free energy. This leads to a periclase melting point of $\sim$ 4180 K at 13 GPa, similar to that determined by previous ab-initio studies (Alfè, 2005). We note that experimental results vary by about 1000 K about this value (3100 – 5373 K at 13 GPa Zerr and Boehler, 1994; Zhang and Fei, 2008). Current thermodynamic models for periclase cannot be extrapolated to the extreme temperatures predicted by the Zhang and Fei (2008) data. However, assuming that the volume change of melting is roughly constant with temperature (1.8 cm^3/mol at 13 GPa), the entropy of melting at

a melting point of 5373 K would be about 50% of that for a melting point of 4180 K (13.25 vs. 27.5 J/K/mol). At 13 GPa and 2000 K, MgO melt would actually be 15 kJ/mol *more* stable as a result of this lower entropy.

The MD-determined entropy of stishovite is significantly lower than the experimentally determined value (Stixrude and Lithgow-Bertelloni, 2011), so we increased the standard state entropy of the melt by 16.5 J/K/mol. Conveniently, we also have a way to test the volumes predicted by the model of de Koker et al. (2013) at around 13 GPa. The experimentally-derived slope of the coesite melting curve is essentially zero at the triple point with stishovite at 13.7 GPa (Zhang et al., 1993). Therefore, from the Clausius-Clapeyron relationship $dT/dP = \Delta V/\Delta S$ the volumes of coesite and SiO_2 melt must be zero at this point. Unfortunately, the MD-derived SiO_2 melt model has its density crossover with coesite about 4 GPa lower. Therefore, we adjusted the bulk modulus and reference pressure so satisfy this constraint, and the volume at zero pressure. The adjustments required here may not be a failing of the MD simulations; it is likely that the coordination changes in the SiO_2 melt require a higher order Birch Murnaghan EoS than that used by (de Koker et al., 2013). Our adjusted model is probably only accurate in a range of about ± 5 GPa around the triple point. The experimental data can also be used to judge the accuracy of the entropy of the SiO_2 melt model. The MD-derived entropy of melting is $\sim$40 J/K/mol at the triple point. This value is in perfect agreement with the value derived from the Clapeyron slope of the stishovite liquidus (Shen and Lazor, 1995). We note that the slope recently proposed by Millot et al. (2015) is much shallower, but their slope is a two parameter Simon's equation fit based on the triple point temperature at 13.7 GPa and the melting point at 500 GPa, and fits the data at 15–100 GPa (Shen and Lazor, 1995; Lyzenga et al., 1983) rather poorly. A Simon's equation fit is probably inappropriate over such extreme pressure ranges, especially where the melting point may be rather sensitive to changes in cation coordination.

3.2.2. Solution model

A subregular solution model was adopted to describe the free energy of intermediate-composition MgO-SiO_2 melts. The two interaction parameters W_{MS} and W_{SM} at 13 GPa were derived from the melt composition at the forsterite (fo)-HP clinoenstatite (hen) eutectic (Presnall et al., 1998) and melting temperatures at the fo, hen and fo-hen cotectic compositions (Presnall and Gasparik, 1990; Presnall and Walter, 1993). We assumed an ideal entropic contribution to mixing. The pressure dependencies were fit to the melting curves. It should be noted that although the excess volumes are similar to the results of de Koker et al. (2013), the excess entropies are some 50% lower. However, they provide an excellent fit to the forsterite and orthoenstatite melting curves (see Supplementary Materials).

3.3. The hydrous melt model

In this study, the anhydrous components in our hydrous melts are normalised to a one-cation basis (i.e. MgO, $Mg_{2/3}Si_{1/3}O_{4/3}$, $Mg_{1/2}Si_{1/2}O_{3/2}$, SiO_2). We follow Silver and Stolper (1985) in determining the proportions of H_2O + O_{br} and OH_{tm} in the melt as a function of the molar proportion of H_2O p_{H_2O} as follows:

$$p' = \frac{p_{H_2O}}{p_{H_2O} + r\,(1. - p_{H_2O})} \tag{6}$$

$$X_O = 1 - p' - \frac{0.5 - \sqrt{0.25 - \frac{K_{(1)}-4}{K_{(1)}}\,(p' - p'^2)}}{\frac{K_{(1)}-4}{K_{(1)}}} \tag{7}$$

$$X_{H_2O} = X_O + 2p' - 1 \tag{8}$$

$$X_{OH} = 1 - X_O - X_{H_2O} \tag{9}$$

p' is the molar proportion of H_2O where the silicate is normalised on a one oxygen basis (rather than a one-cation basis). We assume that all bridging oxygens are equally likely to be protonated. The number of oxygens per formula unit r thus increases monotonously from 1 to 2 across the MgO-SiO_2 binary

($r_{\mathrm{per}} = 1$, $r_{\mathrm{fo,\ wad,\ rw}} = 4/3$, $r_{\mathrm{oen,\ cen}} = 3/2$, and $r_{\mathrm{coe,\ stv}} = 2$). The ideal activities of the anhydrous and water components can then be calculated:

$$a^{s}_{ideal\ melt} = X^{r}_{O} \tag{10}$$

$$a^{H_2O}_{ideal\ melt} = X_{H_2O} \tag{11}$$

The activity coefficients (i.e. the activity prefactor which provides the non-ideal contribution to mixing; $a = \gamma a_{ideal}$) are equal to one except in the case of the MgO-H_2O binary, where a simple Margules model is applied (Hunt and Manning, 2012)

$$RT \ln \gamma_i = {p_j}^2 \left(1 - p_j\right) \left(2W_{ji} - W_{ij}\right) \tag{12}$$

where the subscripts i and j correspond to the components s or H_2O. Equilibrium with the solid can now be found using Equation 5, noting that the dataset-derived values of G^{s}_{solid} of the forsterite (Mg_2SiO_4) and enstatite ($Mg_2Si_2O_6$) polymorphs should be divided by 3 and 4 to reduce them to their one-cation equivalents.

4. Results

4.1. Ex-situ observations

Experimental details and results are shown in Table 2. Superliquidus runs revealed networks of dendritic crystals of brucite, forsterite, enstatite and stishovite. Below the liquidus, solid phases tended to aggregate at the cold end of the capsules. Periclase formed equant crystals often associated with quench overgrowths which appear brighter in BSE images. Forsterite formed tabular crystals about 100 μm long. Enstatite crystals were much smaller, forming ca. 5 μm equant grains. Stishovite also formed equant to blocky grains, but crystals only separated from the melts in chambers with a high water content. In addition to the difference in texture and shape between quench crystals and liquidus phases, subliquidus phases typically contained many small inclusions of Pt-Rh oxides. A typical set of run products is shown in Figure 2.

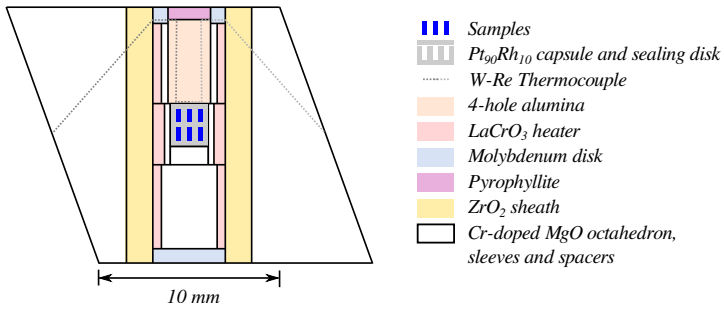

Figure 1: The 18/11 octahedral assembly design used in this study.

Table 2: Experimental run conditions and run products determined by SEM/EDS. Compositions are listed in order of increasing molar H_2O content. Unused compositions for each run are marked by a dash. Minor solids are listed in brackets. Mineral abbreviations are as follows: br - brucite, per - periclase, co - hydroxychondrodite, en - clinoenstatite, s - stishovite. Melts are present in all run products.

Expt #	P (GPa)	T (°C)	t (min)	brucite+PtAc	forsterite+PtAcid	enstatite+PtAcid	quartz+PtAcid	br+q
Z1063	13	1200	40	-/br/br/br/L	co/fo/fo/(fo)	en/en/en/en	-/-/-/-/-/-/-/-	-/-/-/-
Z1085	13	1300	40	-/-/per/L/L	-/fo/(en)/L	-/-/-/-	-/-/-/-/-/-/-/-	-/-/-/-
Z1079	13	1300	35	-/per/per/L/L	fo/fo/en/(en)	en/en/en/en	-/-/-/-/-/-/-/-	-/-/-/-
Z1058	13	1400	30	-/per/(per)/L/L	fo/(fo)/L/L	en/en/en/(en)	-/-/-/-/-/-/-/-	-/-/-/-
Z1060	13	1500	20	-/-/-/-/-	(fo)/L/L/L	en/en/L/L	-/-/-/-/-/-/-/-	-/-/-/-
Z1140	13	1600	10	-/-/-/-/-	-/-/-/-	-/-/-/-	s/s/s/s/s/s/s/(s)	s+en/en/en/en
Z1084	13	1650	10	-/-/-/-/-	-/-/-/-	L/L/-/-	-/-/-/-/-/-/-/-	-/-/-/-
Z1207	13	1700	8	-/-/-/-/-	-/-/-/-	-/-/-/-	s/s/s/s/s/s/(s)/L	s+en/(en)/L/L
Z1209	13	1800	5	-/-/-/-/-	-/-/-/-	-/-/-/-	s/s/s/s/(s?)/L/L/L	s/L/L/L
Z1091	13	1900	5	(per)/-/-/-/-	-/-/-/-	-/-/-/-	-/-/-/L/-/L/L/L	L/L/-/-

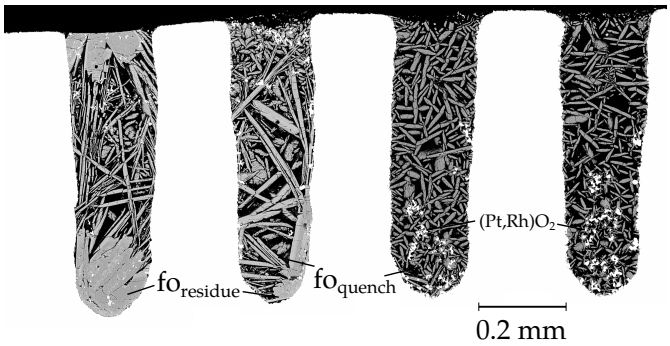

Figure 2: BSE image of typical run products. Experimental chambers from Experiment Z1058, conducted at 1400 °C and 13 GPa. Chambers have compositions along the forsterite-water binary, with water contents increasing from left to right.

4.2. Subsystems

4.2.1. MgO-H_2O

Experimental results for the system MgO-H_2O are shown in Figure 3. The periclase-brucite-water invariant at 13 GPa is well constrained at 62–66 mol% H_2O and ∼1250 °C. The MgO content of the liquid increases gradually with increasing pressure, as a result of the extremely high melting temperature of periclase. In addition to the thermodynamic models described in the methods section, the activity of H_2O at the brucite-periclase-melt triple point is calculated using the thermodynamic dataset of (Holland and Powell, 2011), which includes models for brucite, periclase and water (Pitzer and Sterner, 1995). This provides an additional constraint on the melt model via the equation

$$RT \ln a_{H_2O} = G_{br} - G_{per} - G_{H_2O} \tag{13}$$

The brucite melting curve is obtained by finding the solution to the equation

$$(G_{MgO,melt}+RT \ln a_{MgO})+(G_{H_2O,HP}+RT \ln a_{H_2O}) = G_{br,HP}-G_{per,HP}+G_{per,SLB} \tag{14}$$

where the right hand side is the chemical potential of $Mg(OH)_2$ in the melt, and the right hand side is the Gibbs free energy of brucite with a correc-

tion for the different standard state energies of MgO between the Holland and Powell (2011) and Stixrude and Lithgow-Bertelloni (2011) datasets. $G_{(1)} = RT \ln K_{(1)} = -75000$ J/mol (r=1) provides a good fit to the data if additional asymmetry is added via a binary subregular model (W_{MgO-H_2O}=55000 J/mol, W_{H_2O-MgO}=0 J/mol). The large positive interaction parameter increases the tendency for melt-fluid immiscibility at the water-rich end of the system. This is reflected in the flat slope of the brucite liquidus, and is in excellent agreement with the suggestion that the second critical endpoint in the MgO-H_2O system probably lies at ca. 12–13 GPa (Melekhova et al., 2007).

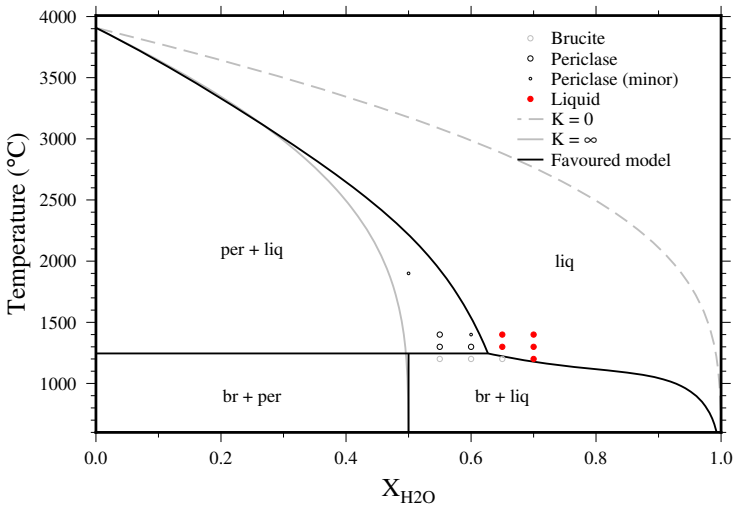

Figure 3: The periclase-water phase diagram at 13 GPa, based on current experimental results. Model fits to the data use the melt formulation of Silver and Stolper (1985), with r=1 and K=K(T) (see discussion in main text). Properties of the anhydrous solid and melt are taken from published literature (Stixrude and Lithgow-Bertelloni, 2011; de Koker et al., 2013). An additional subregular interaction term is required to match the composition and temperature of brucite dehydration.

The dehydration of brucite at high pressure was previously studied by Fukui et al. (2005). They reported that the stability of brucite reaches a maximum at about 9–10 GPa and 1200 °C, decomposing at 1100–1150 °C at 13 GPa. The temperature difference between their study and ours is therefore 50 °C, within experimental uncertainties.

4.2.2. Mg_2SiO_4-H_2O

The melting point depression of forsterite in the presence of water at 13 GPa is illustrated in Figure 4. The model parameters shown are $G_{(1)} = 75 \cdot (1420 - T)$ J/mol, $r = 4/3$. The anhydrous melting of forsterite is incongruent, so at low water contents the liquidus phase along the Mg_2SiO_4-H_2O binary is periclase (see also Figure 7). Water-rich chambers from experiments run at 1300 °C revealed small quantities of enstatite, indicating that the forsterite-enstatite cotectic crosses the Mg_2SiO_4-H_2O tie line at 1300-1400 °C. This is in excellent agreement with results on the wadsleyite-water system run at 15 GPa (Demouchy et al., 2005; Litasov et al., 2011). At 1200 °C, one chamber contained large crystals of hydroxychondrodite. The presence of this MgO-rich phase in the chamber with the lowest water contents may be explained by an MgO-deficit in forsterite resulting from the incorporation of hydrogen via the substitution mechanism $Mg^{2+} \rightarrow 2H^+$ (Keppler and Bolfan-Casanova, 2006). Alternatively it could simply be the result of a small SiO_2 deficit in that sample chamber.

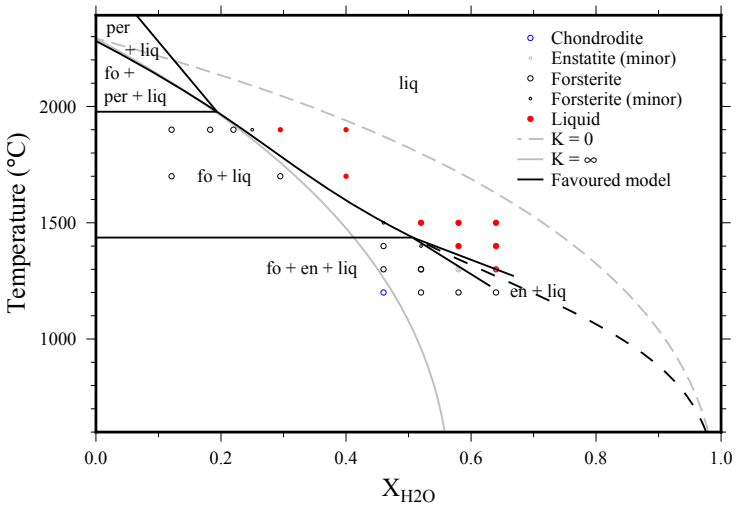

Figure 4: The forsterite-water phase diagram at 13 GPa, based on current experimental results. The thermodynamics of pure forsterite are taken from the literature (Stixrude and Lithgow-Bertelloni, 2011), and the properties of the anhydrous melt are from the mixing model described in the text. At high temperatures, the forsterite liquidus is metastable with respect to periclase + melt. High temperature data come from the study of Novella et al. (2016).

4.2.3. $MgSiO_3$-H_2O

The melting of high pressure clinoenstatite in the presence of water is shown in Figure 5. Unlike the forsterite or periclase liquidi, the observed depression of melting at low water contents exceeds that predicted by even the most extreme commonly-used ideal mixing model, where all oxygens in the melt are equivalent and available for protonation, and molecular H_2O is absent (Silver and Stolper, 1985). The liquidus at higher water contents can be fit well with model parameters $G_{(1)} = 120 \cdot (1750 - T)$ J/mol, $r = 3/2$. The disagreement between this model and the experimental observations is small, and could plausibly be due to experimental error. However, given the results for stishovite (see next section), we feel that more complex models are required to explain the depression of melting in the $MgSiO_3$ system.

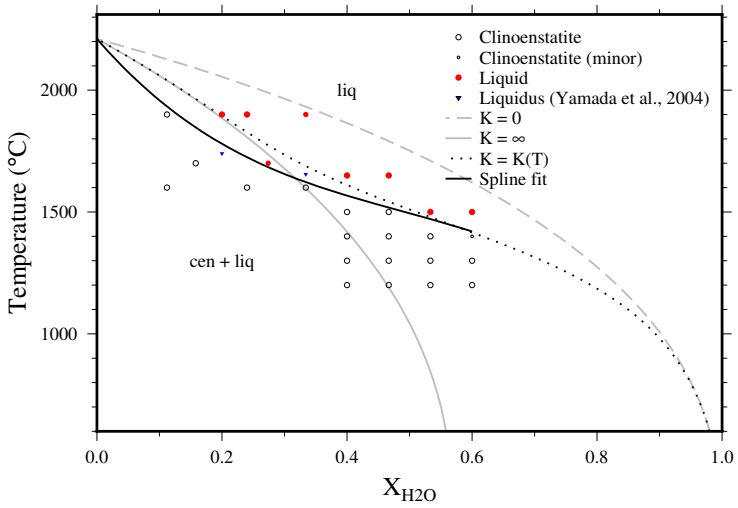

Figure 5: The clinoenstatite-water phase diagram at 13 GPa, based on current experimental results. The thermodynamics of pure high pressure clinoenstatite are taken from the literature (Stixrude and Lithgow-Bertelloni, 2011), and the properties of the anhydrous melt are from the mixing model described in the text. High temperature data come from the study of Novella et al. (2016).

Our experimentally determined liquidus is in excellent agreement with the experimental results of Yamada et al. (2004), as is the absence of stishovite in

any of the sample chambers. We note that although we do not observe any evidence for melt-fluid immiscibility, the flat liquidus at ca. 1500 °C causes a very rapid change from water-rich to water-poor fluids with increasing temperature, in agreement with Inoue (1994) and Yamada et al. (2004). One possibility is that this reflects relatively high water loss from the water rich bulk compositions. However, there is very little evidence for melt loss from the capsules; the lids on the capsules were well-sealed and showed no evidence of melt escape. The implication is that for a given bulk H_2O content, a sharp rise in the degree of partial melting occurs when bulk compositions along the en+H_2O join are heated above 1500 °C.

4.2.4. SiO_2-H_2O

The 13 GPa SiO_2-H_2O binary phase diagram is shown in Figure 6. While the deviation between the predicted enstatite liquidus depression for ideal molecular H_2O-free melts and the experimental observations are relatively small, the deviation for the stishovite data is extreme. The mixing model presented in Figure 6 has parameters $G_{(1)} = 100 \cdot (1200 - T)$ J/mol, $r = 2$ is fit to the extrapolation of the experimentally defined liquiudus, but clearly fails to fit any of the experimental data. There are several possible explanations for this. First, the melting point of anhydrous stishovite (which is metastable with respect to coesite) could be overestimated by ca. 300 °C, or the entropy of melting could be 10–20 J/K/mol, rather than 40 J/K/mol. Neither of these possibilities is very likely; the coesite and stishovite melting curves provide good constraints on the volume and entropy of SiO_2 melt in the region of the triple point at ca. 13.5 GPa. A third possibility is that approximately 30% volume liquidus-phase stishovite crystals were missed during SEM analysis. This is also extremely unlikely; the equant and dendritic morphologies of liquidus and quench stishovite are instantly recognisable, and the thermal gradients in the capsule lead to melt separation on the timescales of the experiments, such that even a small (5%) volume proportion of solids should be detected.

Having ruled out experimental error and uncertainties in the thermodynamics of the anhydrous system, the only possibility is that hydrous SiO_2 melts with relatively low water contents are stabilised well beyond the expected entropic stabilisation from random protonation of the silica network. The causes of this additional stability (and, to a lesser extent, that of hydrous $MgSiO_3$ melts) are well beyond the scope of the current study, but may be a fruitful line of investigation for molecular dynamics simulations (e.g. Karki and Stixrude, 2010).

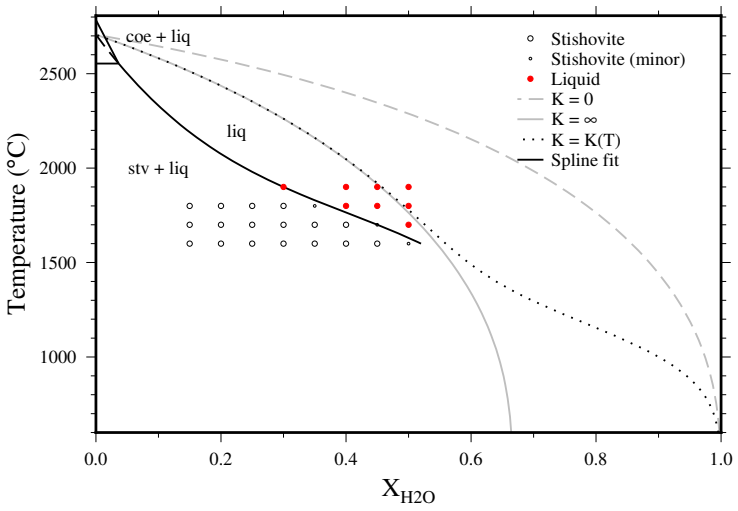

Figure 6: The silica-water phase diagram at 13 GPa, based on current experimental results. The thermodynamics of stishovite and the anhydrous melt are described in the text. At high temperatures, the stishovite liquidus is metastable with respect to coesite and melt.

4.3. The MgO-SiO_2-H_2O system

The set of experimental analyses can be used to create a preliminary ternary liquidus diagram (Figure 7). It should be noted that the periclase liquidus field and periclase-forsterite cotectic are poorly constrained by the data. The low temperature extension of the cotectic is chosen to fit the reported Mg:Si ratios of melts in equilibrium with forsterite and various DHMS phases at 13.5 GPa (Melekhova et al., 2007).

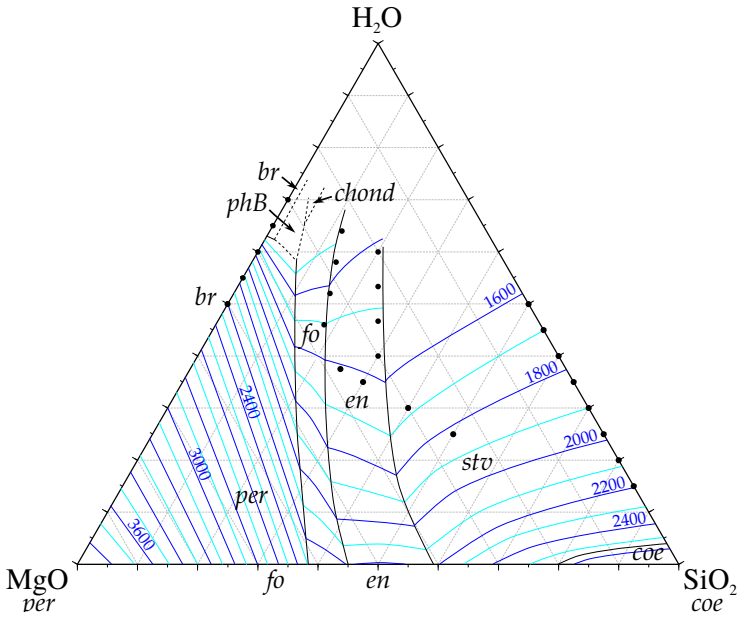

Figure 7: A preliminary ternary liquidus diagram at 13 GPa, based on current experimental results. Contours are in °C, and mineral abbreviations are liquidus fields as follows: per - periclase, fo - forsterite, en - clinoenstatite, stv - stishovite, coe - coesite, phB - phase B, br - brucite, chond - hydroxychondrodite, ice - ice VII. The locations of the contours are constrained by observed liquidus phases and the liquidus-bracketing results presented here. Previous work on hydrous phase stability and Mg:Si ratios for cotectic melts are also included (Melekhova et al., 2007).

5. Discussion

5.1. Melting in deep subduction zones and atop the mantle transition zone

Our melt model in the MSH system serves as a useful tool for investigating melting at high pressures in the mantle. In particular, the forsterite-enstatite cotectic implies that hydrous melts in equilibrium with depleted peridotites at typical mantle temperatures of 1500 °C will contain $\sim$ 48 mol% H_2O and an Mg:Si ratio of about 2 (the same as forsterite), corresponding to about 26 wt% H_2O. Such compositions are far too water-rich to be neutrally buoyant relative to a forsterite + enstatite assemblage (Mookherjee et al., 2008), and will rise through the mantle. Adding further components to the system will modify this behaviour. In particular, the addition of iron lowers anhydrous melting temperatures and increases melt densities. Thus, we cannot directly use our results to confirm or refute the viability of the water-filter model proposed by Bercovici and Karato (2003), which requires neutrally buoyant or dense melts at the 410 km discontinuity. However, the flat liquidus curves revealed by our experiments are likely to also be observed in more natural chemical systems. The current results imply that the water contents of melts in equilibrium with forsterite and enstatite drop from 62 mol% (34 wt%) to around 30 mol% (16 wt%) over a temperature interval of about 400 degrees between 1300 and 1700°C. At $\sim$400 km depth, the interiors of slabs could be as cold as 600-800°C (Frohlich, 2006), while surrounding mantle has a temperature of $\sim$1400°C (Anderson, 1982). Mantle plumes have temperatures up to $\sim$1700°C. The large increases in silicate content in melts at the top of the transition zone would lead to large density and viscosity changes; close to slabs, hydrous melts could be buoyant and inviscid, while in warmer mantle of a similar composition they would be dense and more viscous. Dissolution of silicate material into melt would also promote channelisation of hydrous melts close to the top interface of subducting slabs (Spiegelman et al., 2001; Weatherley and Katz, 2012), which could increase seismic visibility by significantly increasing melt fraction and connectivity of melt.

5.2. Water partitioning in the mantle transition zone

Partitioning of hydrogen between mineral and melt phases can be described using a partition coefficient D:

$$D^{a/b}_{H_2O} = c^a_{H_2O}/c^b_{H_2O} \tag{15}$$

where $c^i_{H_2O}$ is the concentration of H_2O (in wt%) in phase i (Keppler and Bolfan-Casanova, 2006). In quenchable phases, there are a number of ways that concentration can be measured, including FTIR, SIMS and ERDA. In the case of melts, which are unquenchable, $c^{melt}_{H_2O}$ in partitioning studies has most commonly been estimated by mass balance or by assuming that the deficit in microprobe totals is due to hydrogen. In two studies on Fe-free wadsleyite, Demouchy et al. (2005) and Litasov et al. (2011) present estimates of water content in melts calculated from microprobe deficits. A similar study on ringwoodite was undertaken by Ohtani et al. (2000). The T-X_{H_2O} dependencies of the melts in equilibrium with wadsleyite or ringwoodite are strikingly different (Figure 8). For example, melt in equilibrium with wadsleyite at 15 GPa and 1400 °C was estimated to contain 10.6-13.3 wt% H_2O, while melt compositions in equilibrium with ringwoodite at 20 GPa and 1400 °C suggest water contents of 57-66 wt% H_2O. Modelled Mg_2SiO_4 melting temperatures increase by only 40 K between 15 and 20 GPa, and entropies of melting at these two pressures are not very different (92.4 vs. 97 J/K/mol), so unless the thermodynamics of mixing in the liquid change markedly between these pressures, estimates of $c^{melt}_{H_2O}$ for the ringwoodite or wadsleyite studies (or both) must be somewhat inaccurate. We note that two of the three melt compositions in equilibrium with ringwoodite fall above the temperatures indicating that hydrogen exists only as molecular H_2O (Silver and Stolper, 1985). In addition, the calculated liquidus temperatures in the wadsleyite studies at 15 GPa are lower than those reported at 5.5 GPa (Inoue, 1994). Both of these observations appear highly unlikely.

Here, we recalculate the wadsleyite/melt and ringwoodite/melt partitioning values with our melt model, assuming that our fitted values of $G_{(1)}$ and r are suitable between 13 and 20 GPa. We justify this by noting that speciation is

likely to be only weakly dependent on pressure under these conditions. Water concentrations in the solid are taken from the original studies. We restrict our analysis to data from 1100–1400 °C, where the Mg:Si ratios of the melts are similar to that in forsterite. At 15 GPa, $D_{H_2O}^{wad/melt}$ increases from 0.30 to 0.51 between 900 and 1200 °C, and then decreases back to 0.32 at 1400 °C. The three ringwoodite H_2O concentrations (20-23 GPa) indicate a decrease in $D_{H_2O}^{rw/melt}$ from 0.68 to 0.57 between 1300 and ca. 1400 °C.

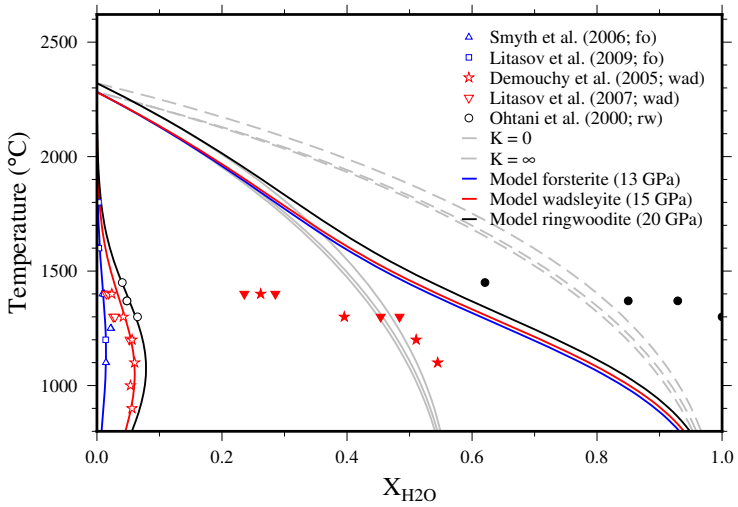

Figure 8: Water concentrations in wadsleyite, ringwoodite and melt, modelled at 15 and 20 GPa. Experimental data is taken from three published studies (Ohtani et al., 2000; Demouchy et al., 2005; Litasov et al., 2011).

We now create thermodynamic models for incorporation of H_2O into forsterite, wadsleyite and ringwoodite. For forsterite, we use high pressure (12–14 GPa) experimental data on the solids from Smyth et al. (2006) and Litasov et al. (2009); neither of these studies estimate coexisting melt compositions. Hydrogen in all three minerals is incorporated as proton pairs substituting for Mg ($Mg^{2+} \leftrightarrow 2H^+$) (Smyth, 1987; Smyth et al., 2003). Ringwoodite potentially also exhibits a substitution involving Si ($Si^{4+} \leftrightarrow Mg^{2+} + 2H^+$) (Kudoh et al., 2000). Both of these reactions may be written in the form

$$H_2O + O = (OH)_2 \tag{16}$$

which leads to the equilibrium relation

$$\Delta G = -RT \ln \left(\frac{a_{(OH)_2}}{a_{H_2O} a_O} \right), \tag{17}$$

$$= \Delta H - (T - T_0)\Delta S + (P - P_0)\Delta V \tag{18}$$

where ΔG is the Gibbs energy associated with the reaction. The second equation is a linearised form of the expression describing the change in free energy with pressure and temperature. The first equation can be simplified by making the approximation that a_O is constant and that the weight percentage of H_2O in the solid c_{H_2O} is proportional to the activity of $(OH)_2$. Both of these assumptions are probably reasonable at low values of c_{H_2O}. Rearranging now produces the expression:

$$c_{H_2O} \propto a_{H_2O} \exp \left(-\frac{\Delta H - (T - T_0)\Delta S + (P - P_0)\Delta V}{RT} \right) \tag{19}$$

Further simplifications can be made by taking $T_0 = 0$ K, by realising that P_0 can be neglected at high pressures, and by incorporating the factor $\Delta S/R$ into the exponential prefactor. Finally, it is recognised that the pressure and temperature dependence of the Gibbs free energy of water G_{H_2O} is highly non-linear. For this reason, we split the Gibbs free energy change of the anhydrous and hydrous solid from that of the liquid, yielding the equation (Keppler and Bolfan-Casanova, 2006):

$$c_{H_2O} = A a_{H_2O} f_{H_2O} \exp \left(-\frac{\Delta H + P\Delta V^{solid}}{RT} \right), \tag{20}$$

$$f_{H_2O} = \exp \left(\frac{\Delta G_{H_2O}}{RT} \right) \tag{21}$$

We calculate the fugacity of pure water f_{H_2O} from the equation of state of (Pitzer and Sterner, 1995). We can now fit the values of A, ΔH and ΔV to the experimental data on forsterite, wadsleyite and ringwoodite using our melt model to provide estimates of a_{H_2O}. The sharp spike in olivine water concentrations at 1250 °C reported by Smyth et al. (2006) is difficult to fit with reasonable enthalpies, but we obtain good fits with the rest of their data, and those of Litasov et al. (2009). The wadsleyite data of Demouchy et al.

Table 3: Thermodynamic models for water solubility in wadsleyite and ringwoodite

Phase	P_{ref} (Pa)	A [kg/(kgPa)]	$\Delta H_{P_{ref}}$ [J/mol]	ΔV [m^3/mol]
Olivine	1.2e10	3.23e-12	1.50e5	1e-5
Wadsleyite	1.5e10	1.97e-12	1.60e5	1e-5
Ringwoodite	2.0e10	1.46e-12	2.03e5	1e-5 (fixed)

(2005) at 1200 °C and 14–17 GPa are consistent with a low pressure effect on water content, implying that $\Delta V \sim 10^{-5}$ m^3/mol, similar or slightly lower than estimates for olivine (1.00 – 1.06 $\cdot 10^{-5}$ m^3/mol Kohlstedt et al., 1996; Zhao et al., 2004; Mosenfelder et al., 2006). A single data point at 18 GPa has much lower water contents, which would require $\Delta V \sim 1.25 \cdot 10^{-5}$ m^3/mol. This value is inconsistent with the large water contents at 16 and 17 GPa, and is probably unreasonable given the reported values for olivine. We therefore favour the lower estimate of ΔV, and assume the same value for ringwoodite. The model values are shown in Table 3.

These models allow us to predict the partition coefficients of water between olivine, wadsleyite and melt at the 410 km discontinuity (∼14 GPa; Figure 9), and wadsleyite, ringwoodite and melt at the 520 km discontinuity (∼18 GPa; Figure 10). $D_{H_2O}^{wad/fo}$ displays a decrease from ∼4 at 1000 °C to ∼1.8 at 2000 °C, in good agreement with the estimates of Litasov et al. (2011) at low temperatures, but without a return to high values at high temperatures, where water contents are lower and prone to large relative errors. $D_{H_2O}^{ring/wad}$ decreases from ∼1.4 at 1000 °C to ∼1.1 at 2000 °C. These values imply that upwelling across both the 410 and the 520 km discontinuity will cause partial melting. Both boundaries have been associated with low seismic velocities, which may indicate zones of deep melting (e.g. Jasbinsek et al., 2010). The small temperature dependence on the wadsleyite-ringwoodite partition coefficient implies that repartitioning of water during secular cooling within the mantle transition zone is likely to be more minor (and in the opposite direction) to that proposed by Demouchy et al. (2005).

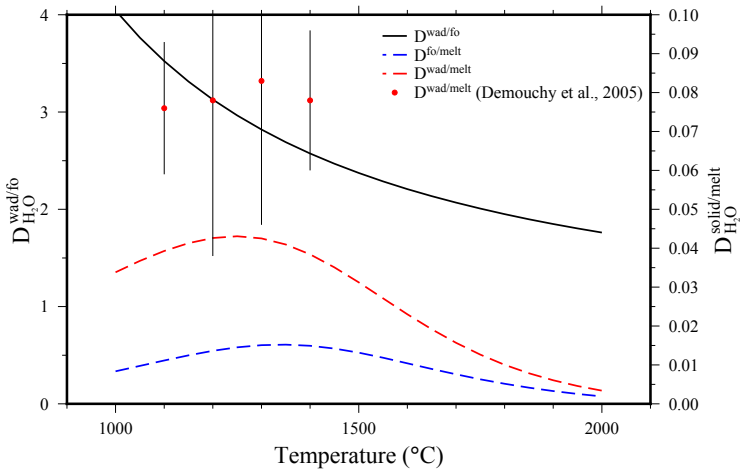

Figure 9: Modelled H_2O partition coefficient between forsterite, wadsleyite and melt at 14 GPa, approximately the pressure of the 410 km discontinuity. Note the separate scales for solid/solid and solid/melt partitioning. The difference in melt compositions between this study and that of Demouchy et al. (2005) results in much lower $D^{wad/melt}$ coefficients. Error bars on the wadsleyite datapoints are those reported by Demouchy et al. (2005).

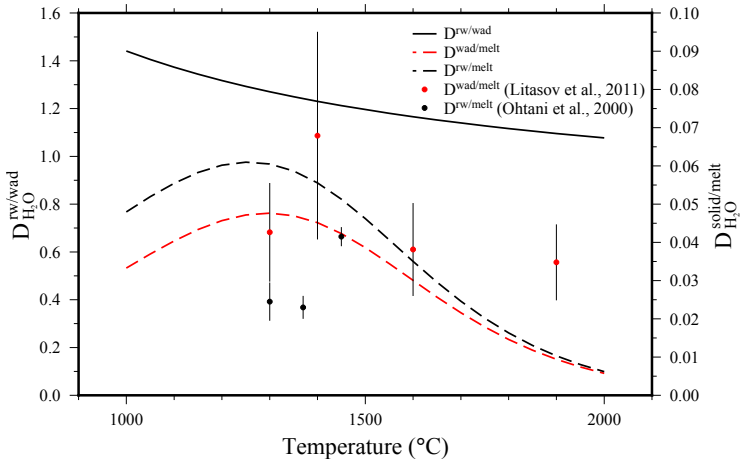

Figure 10: Modelled H_2O partition coefficient between wadsleyite, ringwoodite and melt at 18 GPa, approximately the pressure of the 520 km discontinuity. Note the separate scales for solid/solid and solid/melt partitioning. Error bars on the ringwoodite data points indicate the range of values reported by Ohtani et al. (2000). Error bars on the wadsleyite data points indicate 1 s.d. uncertainties as reported by Litasov et al. (2011).

6. Concluding Remarks

In this study, we have conducted multi-anvil experiments to constrain the topology of the liquidus in the MgO-SiO_2-H_2O system at 13 GPa. We employ a simple thermodynamic model to predict the activities of water in hydrous melts in equilibrium with the mantle, and to create models for incorporation of water into forsterite, wadsleyite and ringwoodite.

We hope that this work forms the foundation for more detailed thermodynamic models of hydrous mantle melts. Particularly intriguing are the concave up topologies of the forsterite, enstatite and stishovite liquidus surfaces, and the large depression of the melting point at low water contents in silica-rich systems. Both of these observations imply efficient hydroxylation of the silicate network and strong interactions between species, which would be interesting subjects for molecular dynamic studies. We also hope that a combination of our liquidus constraints with parameterisations for density and viscosity will be used to inform more realistic models of melt migration above the mantle transition zone and during subduction.

7. Acknowledgements

The authors would like to thank Gerti Gollner for acquiring capsule materials, Stefan Übelhack and Heinz Fischer for assembly and capsule cutting and Hubert Schulze for sample preparation. RM was supported by a Humboldt Postdoctoral Fellowship. This study was funded by the ACCRETE project (European Research Council Advanced Grant, contract number 290568).

References

Alfè, D., 2005. Melting Curve of MgO from First-Principles Simulations. Physical Review Letters 94, 235701.

Anderson, O.L., 1982. The Earth's Core and the Phase Diagram of Iron. Philosophical Transactions of the Royal Society of London Series A 306, 21–35.

Bercovici, D., Karato, S.i., 2003. Whole-mantle convection and the transition-zone water filter. Nature 425, 39–44.

Cottaar, S., Heister, T., Rose, I., Unterborn, C., 2014. BurnMan: A lower mantle mineral physics toolkit. Geochemistry, Geophysics, Geosystems 15, 1164–1179.

de Koker, N., Karki, B.B., Stixrude, L., 2013. Thermodynamics of the MgO-SiO_2 liquid system in Earth's lowermost mantle from first principles. Earth and Planetary Science Letters 361, 58–63.

Demouchy, S., Deloule, E., Frost, D.J., Keppler, H., 2005. Pressure and temperature-dependence of water solubility in Fe-free wadsleyite. American Mineralogist 90, 1084–1091.

Frohlich, C., 2006. A simple analytical method to calculate the thermal parameter and temperature within subducted lithosphere. Physics of the Earth and Planetary Interiors 155, 281–285.

Frost, D.J., Poe, B.T., Trønnes, R.G., Liebske, C., Duba, A., Rubie, D.C., 2004. A new large-volume multianvil system. Physics of the Earth and Planetary Interiors 143, 507–514.

Fukui, H., Inoue, T., Yasui, T., Katsura, T., Funakoshi, K.i., Ohtaka, O., 2005. Decomposition of brucite up to 20 GPa: evidence for high MgO-solubility in the liquid phase. European Journal of Mineralogy 17, 261–267.

Hirschmann, M.M., 2006. Water, Melting, and the Deep Earth H_2O Cycle. Annual Review of Earth and Planetary Sciences 34, 629–653.

Holland, T.J.B., Powell, R., 2011. An improved and extended internally consistent thermodynamic dataset for phases of petrological interest, involving a new equation of state for solids. Journal of Metamorphic Geology 29, 333–383.

Hunt, J.D., Manning, C.E., 2012. A thermodynamic model for the system SiO_2-H_2O near the upper critical end point based on quartz solubility experiments at 500-1100 °C and 5–20 kbar. Geochemica and Cosmochemica Acta 86, 196–213.

Inoue, T., 1994. Effect of water on melting phase relations and melt composition in the system Mg_2SiO_4–$MgSiO_3$–H_2O up to 15 GPa. Physics of the Earth and Planetary Interiors 85, 237–263.

Jasbinsek, J.J., Dueker, K.G., Hansen, S.M., 2010. Characterizing the 410 km discontinuity low-velocity layer beneath the LA RISTRA array in the North American Southwest. Geochemistry, Geophysics, Geosystems 11, n/a–n/a. Q03008.

Karki, B.B., Stixrude, L., 2010. First-Principles Study of Enhancement of Transport Properties of Silica Melt by Water. Physical Review Letters 104, 215901.

Keppler, H., Bolfan-Casanova, N., 2006. Thermodynamics of water solubility and partitioning. Reviews in Mineralogy and Geochemistry 62, 193–230.

Keppler, H., Frost, D.J., 2005. Introduction to minerals under extreme conditions, in: Miletich, R. (Ed.), Mineral Behaviour at Extreme Conditions. EMU. volume 7 of *European Mineralogical Union Lecture Notes in Mineralogy*, pp. 1–30.

Kohlstedt, D.L., Keppler, H., Rubie, D.C., 1996. Solubility of water in the α, β and γ phases of $(Mg,Fe)_2SiO_4$. Contributions to Mineralogy and Petrology 123, 345–357.

Komabayashi, T., Omori, S., Maruyama, S., 2005. Experimental and theoretical study of stability of dense hydrous magnesium silicates in the deep upper mantle. Physics of the Earth and Planetary Interiors 153, 191209.

Kudoh, Y., Kuribayashi, T., Mizobata, H., Ohtani, E., 2000. Structure and cation disorder of hydrous ringwoodite, γ-$Mg_{1.89}Si_{0.98}H_{0.30}O_4$. Physics and Chemistry of Minerals 27, 474–479.

Litasov, K.D., Shatskiy, A., Ohtani, E., Katsura, T., 2011. Systematic study of hydrogen incorporation into Fe-free wadsleyite. Physics and Chemistry of Minerals 38, 75–84.

Litasov, K.D., Shatskiy, A.F., Katsura, T., Ohtani, E., 2009. Water solubility in forsterite at 8-14 GPa. Doklady Earth Sciences 425, 432–435.

Lyzenga, G.A., Ahrens, T.J., Mitchell, A.C., 1983. Shock temperatures of SiO_2 and their geophysical implications. Journal of Geophysical Research 88, 2431–2444.

Melekhova, E., Schmidt, M.W., Ulmer, P., Pettke, T., 2007. The composition of liquids coexisting with dense hydrous magnesium silicates at 11–13.5 GPa and the endpoints of the solidi in the MgO-SiO_2-H_2O system. Geochemica and Cosmochemica Acta 71, 3348–3360.

Millot, M., Dubrovinskaia, N., Černok, A., Blaha, S., Dubrovinsky, L., Braun, D.G., Celliers, P.M., Collins, G.W., Eggert, J.H., Jeanloz, R., 2015. Shock compression of stishovite and melting of silica at planetary interior conditions. Science 347, 418–420.

Mookherjee, M., Stixrude, L., Karki, B., 2008. Hydrous silicate melt at high pressure. Nature 452, 983–986.

Mosenfelder, J.L., Deligne, N.I., Asimow, P.D., Rossman, G.R., 2006. Hydrogen incorporation in olivine from 2–12 GPa. American Mineralogist 91, 285–294.

Nagano, Y., 2002. Standard enthalpy of formation of platinic acid. The Journal of Chemical Thermodynamics 34, 1745–1750.

Novella, D., Dolejs, D., Myhill, R., Pamato, M., Manthilake, G., Frost, D.J., 2016. Melting phase relations in the systems Mg_2SiO_4-H_2O and $MgSiO_3$-H_2O

at upper mantle conditions. Geochimica et Cosmochimica Acta, under review .

Ohtani, E., Mizobata, H., Yurimoto, H., 2000. Stability of dense hydrous magnesium silicate phases in the systems Mg_2SiO_4-H_2O and $MgSiO_3$-H_2O at pressures up to 27 GPa. Physics and Chemistry of Minerals 27, 533–544.

Pearson, D.G., Brenker, F.E., Nestola, F., McNeill, J., Nasdala, L., Hutchison, M.T., Matveev, S., Mather, K., Silversmit, G., Schmitz, S., Vekemans, B., Vincze, L., 2014. Hydrous mantle transition zone indicated by ringwoodite included within diamond. Nature 507, 221–224.

Pitzer, K., Sterner, S., 1995. Equations of state valid continuously from zero to extreme pressures with H_2O and CO_2 as examples. International Journal of Thermophysics 16, 511518.

Poli, S., Schmidt, M.W., 2002. Petrology of Subducted Slabs. Annual Review of Earth and Planetary Sciences 30, 207–235.

Presnall, D.C., Gasparik, T., 1990. Melting of enstatite ($MgSiO_3$) from 10 to 16.5 GPa and the forsterite (Mg_2SiO_4)-majorite ($MgSiO_3$) eutectic at 16.5 GPa: Implications for the origin of the mantle. Journal of Geophysical Research: Solid Earth 95, 15771–15777.

Presnall, D.C., Walter, M.J., 1993. Melting of forsterite, Mg_2SiO_4, from 9.7 to 16.5 GPa. Journal of Geophysical Research 98, 19777.

Presnall, D.C., Weng, Y.H., Milholland, C.S., Walter, M.J., 1998. Liquidus phase relations in the system MgO-MgSiO $_3$ at pressures up to 25 GPa: constraints on crystallization of a molten Hadean mantle. Physics of the Earth and Planetary Interiors 107, 83–95.

Shen, A., Keppler, H., 1995. Infrared spectroscopy of hydrous silicate melts to 1000 degrees C and 10 kbar; direct observation of H_2O speciation in a diamond-anvil cell. American Mineralogist 80, 1335–1338.

Shen, G., Lazor, P., 1995. Measurement of melting temperatures of some minerals under lower mantle pressures. Journal of Geophysical Research 100, 17699.

Silver, L., Stolper, E., 1985. A Thermodynamic Model for Hydrous Silicate Melts. Journal of Geology 93, 161–177.

Smyth, J.R., 1987. β-Mg_2SiO_4: a potential host for water in the mantle? American Mineralogist 72, 1051–1055.

Smyth, J.R., Frost, D.J., Nestola, F., Holl, C.M., Bromiley, G., 2006. Olivine hydration in the deep upper mantle: Effects of temperature and silica activity. Geophysical Research Letters 33, 15301. L15301.

Smyth, J.R., Holl, C.M., Frost, D.J., Jacobsen, S.D., Langenhorst, F., McCammon, C.A., 2003. Structural systematics of hydrous ringwoodite and water in Earths interior. American Mineralogist 88, 1402–1407.

Spiegelman, M., Kelemen, P.B., Aharonov, E., 2001. Causes and consequences of flow organization during melt transport: The reaction infiltration instability in compactible media. Journal of Geophysical Research 106, 2061–2077.

Stixrude, L., Lithgow-Bertelloni, C., 2011. Thermodynamics of mantle minerals - II. Phase equilibria. Geophysical Journal International 184, 1180–1213.

Stolper, E., 1982. The speciation of water in silicate melts. Geochemica Cosmochemica Acta 46, 2609–2620.

Tenner, T.J., Hirschmann, M.M., Humayun, M., 2012. The effect of H_2O on partial melting of garnet peridotite at 3.5 GPa. Geochemistry, Geophysics, Geosystems 13, 3016.

Weatherley, S.M., Katz, R.F., 2012. Melting and channelized magmatic flow in chemically heterogeneous, upwelling mantle. Geochemistry, Geophysics, Geosystems 13. Q0AC18.

Yamada, A., Inoue, T., Irifune, T., 2004. Melting of enstatite from 13 to 18 GPa under hydrous conditions. Physics of the Earth and Planetary Interiors 147, 4556.

Zerr, A., Boehler, R., 1994. Constraints on the melting temperature of the lower mantle from high-pressure experiments on MgO and magnesiowüstite. Nature 371, 506–508.

Zhang, J., Liebermann, R.C., Gasparik, T., Herzberg, C.T., Fei, Y., 1993. Melting and subsolidus relations of SiO_2 at 9–14 GPa. Journal of Geophysical Research: Solid Earth 98, 19785–19793.

Zhang, L., Fei, Y., 2008. Melting behavior of (Mg,Fe)O solid solutions at high pressure. Geophysical Research Letters 35, 13302.

Zhao, Y.H., Ginsberg, S.B., Kohlstedt, D.L., 2004. Solubility of hydrogen in olivine: dependence on temperature and iron content. Contributions to Mineralogy and Petrology 147, 155–161.